


Emerging current-voltage plateaus caused by high internal electric potentials in interband cascade photodetectors

A. Bader^{1,*}, F. Rothmayr², N. Khan,² J. Koeth,² A. Pfenning,¹ G. Bastard,^{1,3} S. Höfling¹, and F. Hartmann^{1,†}

¹*Physikalisches Institut, Lehrstuhl für Technische Physik, Julius-Maximilians-Universität Würzburg, Am Hubland, 97074 Würzburg, Germany*

²*nanoplus Advanced Photonics Gerbrunn GmbH, Oberer Kirschberg 4, 97218 Gerbrunn, Germany*

³*Physics Department, Ecole Normale Supérieure - PSL, 24 rue Lhomond, 75005 Paris, France*

 (Received 25 September 2023; revised 10 November 2023; accepted 16 November 2023; published 18 December 2023)

We observe that under illumination and at cryogenic temperatures, plateaus emerge in the current-voltage characteristic of non-photocurrent-matched interband cascade infrared photodetectors (ICIPs) with identical thickness of individual superlattice absorbers. We attribute these plateaus to the formation of internal electric potentials on the order of multiple millivolts originating from a gradually decreasing photocurrent in optically deeper stages caused by light attenuation. At elevated temperatures, the plateaus vanish once the dark current exceeds the maximum photocurrent. Contrarily, in a photocurrent-matched ICIP architecture, with individual absorber thicknesses increasing towards optically deeper stages, no additional internal potentials are formed under illumination. The plateaus are found to show a strong wavelength and bias dependence related to the dispersion of the absorption coefficient of the type-II-InAs/GaSb-superlattice absorbers used. This could potentially be implemented in a two-color-detector approach that allows separation of different spectral bands by biasing of the ICIP.

DOI: [10.1103/PhysRevApplied.20.064033](https://doi.org/10.1103/PhysRevApplied.20.064033)

I. INTRODUCTION

Since their introduction in 2005 [1], interband cascade infrared (IR) photodetectors (ICIPs) have attracted much interest for IR detection systems. They typically use type-II-superlattice (T2SL) absorbers [2–4] based on GaSb/InAs superlattices but can also use AlSb barriers and ternary [5–7] and quaternary [8] alloys. This allows the tailoring of the effective band gap of the ICIP over a wide range from short-wavelength IR to mid-wavelength IR (MIR) and very-long-wavelength IR [9–13]. This enables the potential use of ICIPs in various different applications, such as gas sensing [14–16] or thermal imaging [17]. Dividing the absorber material into multiple individual shorter absorbers and connecting them by means of unipolar barriers mitigates diffusion-length limitations in these MIR detectors [18] and allows efficient extraction of photogenerated carriers under photovoltaic operation [1,12]. Compared with single-stage detectors, the multi-stage architecture also reduces dark currents, resulting in increased detectivity [19]. Because of this, ICIPs are a viable alternative to established photodetectors based on HgCdTe devices, with some ICIPs already outperforming

commercially available uncooled HgCdTe photodetectors with a similar cutoff wavelength [20]. There are significant efforts to increase the operation temperature of T2SL-based photodetectors and ICIPs towards high operating temperature [19–22]. In addition, electrical gain exceeding unity was observed in high-temperature operation of non-photocurrent-matched ICIPs [20,23] caused by light attenuation. However, because of increased noise at elevated temperatures, the best detector performance is achieved at cryogenic temperatures. For applications that require high detectivity with a low noise floor, it is therefore imperative to understand the optical response and carrier dynamics of ICIPs at low or even cryogenic temperatures. For that reason, in the following, low-temperature characteristics of ICIPs are investigated.

II. SAMPLE DESIGN AND GROWTH

A band-structure calculation of one cascade stage of the investigated four-stage ICIP4-375 is shown in Fig. 1(a). The individual absorbers are of equal thickness (not photocurrent matched) and consist of 77 periods (375 nm thick) each of a not-intentionally-doped InAs(2.73 nm)/GaSb(2.14 nm) superlattice and are separated by unipolar hole and electron barriers. Photogenerated electrons are extracted from the absorber over a hole barrier that is composed of seven InAs quantum wells

*andreas.bader@physik.uni-wuerzburg.de

†fabian.hartmann@physik.uni-wuerzburg.de

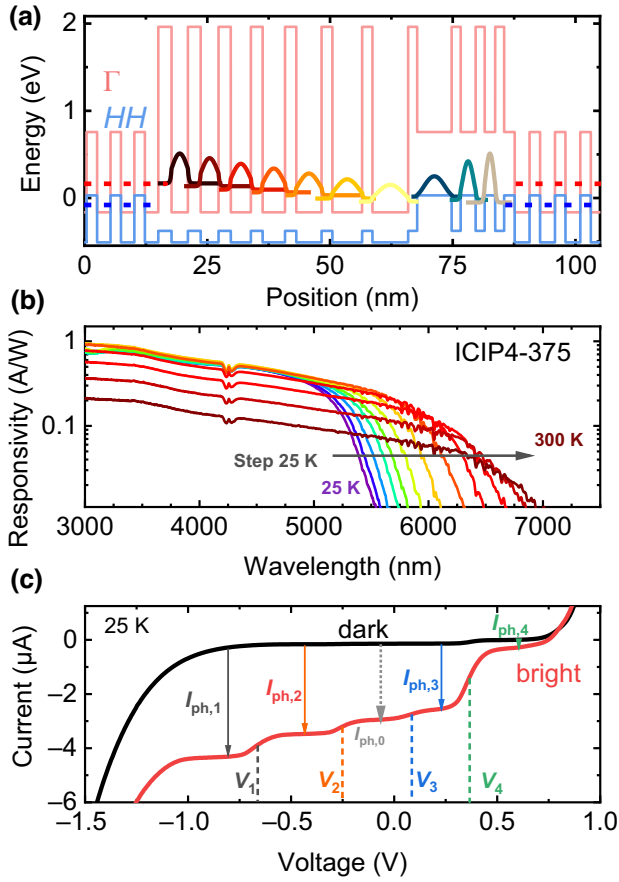


FIG. 1. (a) Band-profile calculation of the unipolar barriers inserted between two superlattice absorbers under flatband condition. The dashed red and blue lines indicate the electron and hole ground states in the superlattice absorber, respectively. (b) Zero-bias responsivity of ICIP4-375 at temperatures between 25 and 300 K. The cutoff wavelength λ_C increases from 5.5 to 7.0 μm . (c) Current measured under dark conditions and under illumination with an MIR Global light source at a sample temperature of 25 K. Plateaus and steps in the current emerge under illumination.

(QWs, in bold) between AlSb barriers (in italics) with thicknesses of (2.70/**3.33**/2.60/**3.64**/2.50/**4.09**/2.40/**4.55**/2.30/**5.15**/2.20/**6.06**/2.20/**7.27**) nm. This forms an electron staircase allowing rapid extraction of photogenerated carriers on the picosecond timescale [1,12]. Holes are extracted over an electron barrier that consists of three GaSb QWs with thicknesses of 7.02, 3.05, and 2.14 nm sandwiched between 1.84-nm-thick AlSb barriers to extract holes from the adjacent absorber. Extracted electrons and holes then recombine at the semimetallic interface between the last InAs QW of the hole barrier and the last GaSb QW of the electron barrier.

The ICIP was grown by molecular beam epitaxy (MBE) on a *p*-doped GaSb substrate with use of standard effusion cells for the group-III elements Ga, Al, and In, and valved crackers for the group-V elements As and Sb. Preceding the actual ICIP structure, a 200-nm-thick

p-doped GaSb:Be buffer was grown with a doping concentration of $3 \times 10^{18} \text{ cm}^{-3}$ matching the substrate doping concentration. After the four cascade stages, the heterostructure was terminated with a 30-nm *n*-doped InAs:Si contact layer with a doping concentration of $2.5 \times 10^{19} \text{ cm}^{-3}$. After growth, the sample was processed into cylindrical mesa structures with diameters between 40 and 540 μm by standard optical lithography and citric acid-based wet chemical etching followed by a sidewall passivation step using an $(\text{NH}_4)_2\text{S}$ solution. Afterwards the sample underwent a second passivation step by sputter deposition of Si_3N_4 and SiO_2 to reduce surface leakage currents and to protect the surface from environmental influences. The sample was then wire-bonded to a chip carrier for measurements.

III. MEASUREMENTS AND RESULTS

The fabricated sample was mounted in a liquid-helium-flow cryostat equipped with a ZnSe window for optical access. The ICIP mesa had diameter $d_{\text{ICIP4-375}} = 478 \mu\text{m}$ and was illuminated with an MIR Global light source. The spectra were normalized with use of a thermal deuterated triglycine sulfate (DTGS) detector and then calibrated to the zero-bias responsivity $R_\lambda = 0.11 \text{ A/W}$ of the device under variable-power laser illumination at a wavelength of 5270 nm at room temperature. Figure 1(b) shows the spectral responsivity R_λ of the device at zero bias and for temperatures between 25 and 300 K. Broadband responsivity was achieved and the cutoff wavelength λ_C shifted from 5.5 μm at 25 K to 6.9 μm at 300 K. The reduced responsivity for temperatures $T \geq 225 \text{ K}$ is most likely caused by a shorter carrier diffusion length. For diffusion lengths below 375 nm (individual absorber length), the collection efficiency of photogenerated carriers is reduced. For electrical characterization of the device, current-voltage (I - V) characteristics were measured. This is shown exemplarily in Fig. 1(c) for a sample temperature of 25 K.

A. Formation of current-voltage plateaus under illumination

For forward bias and for small reverse bias, the dark current I_{dark} follows a diodelike characteristic. For larger reverse bias at $V = V_Z = -1.0 \text{ V}$, however, a Zener-like breakdown is observed with a strong increase in dark current. Under illumination, steps in the current I_{illu} are observed for small positive and negative bias. For larger negative and positive bias, I_{illu} approaches I_{dark} . We attribute the characteristic under illumination to the build up of internal electrical fields based on the framework developed by Huang *et al.* [20], who investigated the electrical gain in interband cascade infrared photodetectors at high temperatures. In non-photocurrent-matched ICIPs, where all absorbers have the same thickness, the photocurrent generated in each stage, $I_{ph,i}$, declines

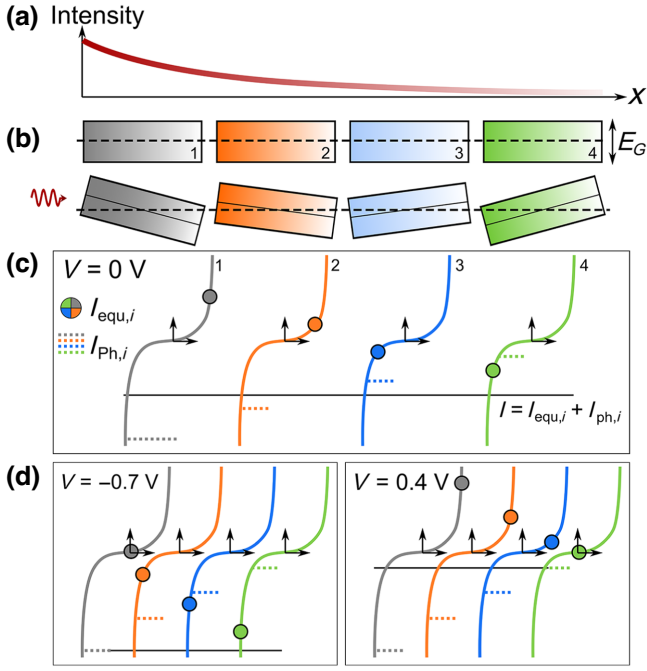


FIG. 2. Emergence of plateaus in the I - V characteristic under illumination. (a) Light intensity attenuates towards optically deeper stages due to absorption. (b) Imbalance in the photocurrent in individual stages leads to the formation of internal electric potentials to offset or supplement the individual photocurrents to maintain current continuity across all stages. (c) The measured total current is the sum of photocurrent $I_{ph,i}$ and the current $I_{equ,i}$ that results from the internal potentials in each stage assuming each stage has a Zener-like characteristic. (d) Reverse biasing the ICIP will compensate the forward potentials, which results exemplarily in measuring $I_{ph,1}$ at $V = -0.7$ V. Forward biasing the ICIP will compensate the reverse electric potentials, resulting in exemplarily measuring the smallest photocurrent, $I_{ph,4}$, at a forward bias of $V = 0.4$ V.

towards optically deeper stages due to light attenuation by absorption of incident radiation in the optically preceding stages, i.e., $I_{ph,1} > I_{ph,2} > \dots > I_{ph,m}$. This is shown schematically in Fig. 2(a). As all four stages are connected in series, the total current in individual stages needs to be identical, $I_1 = I_2 = \dots = I_m$, to maintain current continuity. To achieve this, the photocurrent in all stages will be offset or supplemented by some equalization current $I_{equ,i}$. In optically first stages, the photocurrent (e.g., $I_{ph,1}$, $I_{ph,2}$) will be offset by an internal forward electric potential that emerges opposing the current flow [20]. The photocurrent in the optically deeper stages (e.g., $I_{ph,3}$, $I_{ph,4}$) will be supplemented by a current caused by a reverse electric potential. This is shown schematically in Fig. 2(b). Under zero bias $V = 0$, the sum over all internal potentials V_i must be zero.

Application of a reverse bias will partially compensate the internal forward potentials and the current will increase once V_2 (or V_1) is compensated, allowing the full $I_{ph,2}$ (or $I_{ph,1}$) to flow. Similarly, application of a forward bias will

first compensate the internal reverse electric potential V_3 , which was supplementing $I_{ph,3}$. This results in a reduction of total current. Further increase of the forward bias will eventually compensate the larger V_4 , resulting in a further reduction of the total current. For bias voltages in between different V_i , the total current does not change significantly, resulting in the formation of plateaus in the current-voltage plane. In their model, Huang *et al.* [20] assumed a diode-like characteristic where the current in each stage of the ICIP follows the equation

$$I_i = I_{ph,i} - I_0(e^{qV_i/k_B T} - 1), \quad (1)$$

where I_0 is the saturation dark current, which is assumed to be equal in all stages, as they all share the same superlattice composition and thickness, and T , q , and k_B are the absolute temperature, the elementary charge, and Boltzmann's constant, respectively. At zero bias, the total current in the ICIP is limited by the optically deepest stage (lowest photocurrent), in which the photocurrent is supplemented by a current caused by a reverse electric potential. On the basis of Eq. (1) with $V_4 < 0$, the photocurrent can, at most, be supplemented by I_0 . At high temperatures, this leads to significant gain in ICIPs [20]. At low temperatures, however, $I_0 \ll I_{ph,4}$ and the thermal current supplementing the photocurrent is negligible. In our case, however, the current-voltage characteristic deviates from a diodelike characteristic as a Zener-like breakthrough is observed. Because of this, Eq. (1) does not hold true. We can understand our four-stage ICIP as a series connection of four Zener-like diodes that all have a Zener voltage of around $v_z \approx V_Z/4$. This is indicated in Fig. 2(c) for the $V = 0$ V case. Because of this, the photocurrent of stages that experience a reverse electric potential under illumination can be supplemented by a current I_{Zener} that significantly exceeds I_0 . Under illumination at zero bias, stages 1 and 2 experience a forward electric potential, while in stages 3 and 4, a reverse electric potential emerges. The total measured current therefore is

$$\begin{aligned} I &= I_i = I_{ph,1,2} + I_0(e^{qV_{1,2}/k_B T} - 1) \\ &= I_{ph,3,4} + I_0(e^{qV_{3,4}/k_B T} - 1) + I_{Zener,3,4} \end{aligned}$$

At a reverse bias of $V = -0.7$ V, the external field is large enough to compensate the internal forward potential V_1 , resulting in $I = I_{ph,1}$. At a forward bias of $V = 0.4$ V, the external field is large enough to compensate the internal reverse electric potential V_4 , and $I = I_{ph,4}$. These example cases are shown in Fig. 2(d). Whenever the external bias is sufficient to compensate internal fields, a step in the photocurrent is observed.

B. Temperature dependence

To further investigate the formation of plateaus, I - V characteristics were measured under dark conditions, as

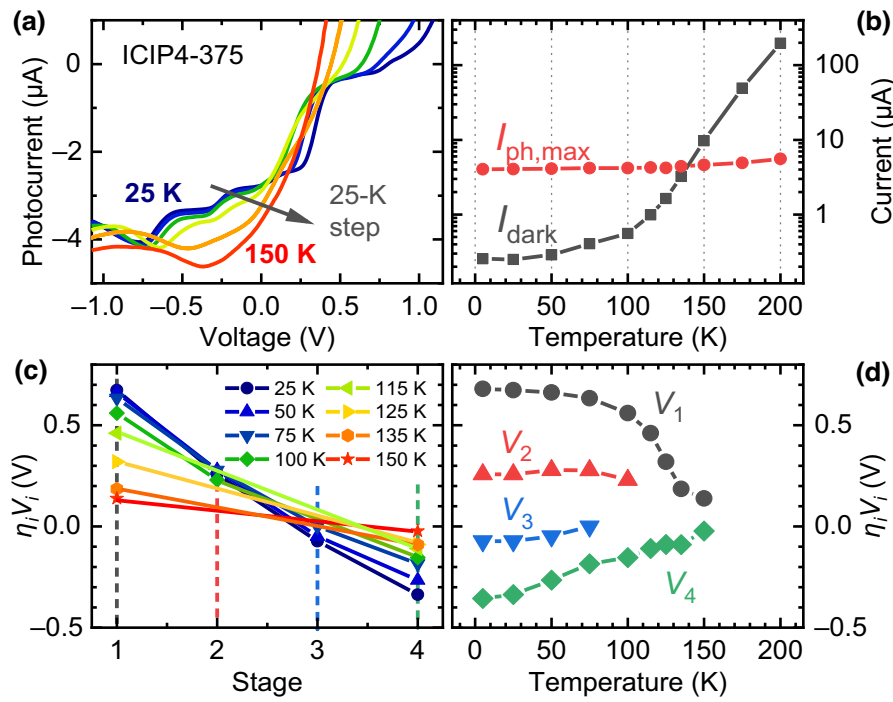


FIG. 3. (a) Photocurrent of ICIP4-375 under broadband MIR illumination at different temperatures. Four steps in the photocurrent and a local maximum can be observed. (b) Maximum photocurrent $I_{\text{ph,max}}$ and dark current at different sample temperatures. At 150 K, the dark current exceeds $I_{\text{ph,max}}$ by a factor of 2. (c) Evolution of $\eta_i V_i$ at different temperatures. (d) $\eta_i V_i$ as a function of sample temperature. At temperatures above 150 K, all steps in the photocurrent and plateaus vanish.

well as under illumination with a broadband MIR Global light source at different temperatures. The total photocurrent $I_{\text{ph}} = I_{\text{illu}} - I_{\text{dark}}$ was calculated by subtracting the dark current I_{dark} from the measured current under illumination I_{illu} . The photocurrent at different temperatures is shown in Fig. 3(a).

At four distinctive external bias voltages, the photocurrent increases in a steplike manner, indicating the successive compensation of the four internal electric potentials V_i . Once the external reverse bias is sufficient to compensate V_1 , the unadulterated $I_{\text{ph},1}$ flows and a global maximum in the photocurrent can be observed as the photocurrent is highest in the optically first stage. The external bias voltage needed to compensate the individual internal electric potentials V_i is correlated to the differential resistance of individual stages R_i , i.e., $V = ((\sum(R_i))/R_i)V_i = \eta_i V_i$. Thus, if all stages have a similar resistance $R_1 \approx R_2 \approx \dots \approx R_m$, the applied voltage drops equally across all stages, resulting in $\eta_i = m$ ($\eta_i = 4$ for four stages). If R_i of one stage is considerably higher than the differential resistance of the other stages, then most of the applied bias drops across this i th stage and $\eta_i \approx 1$.

From Fig. 3(a) it can be seen that with increasing sample temperature, the plateaus become less pronounced and vanish at a temperature of around 150 K.

Huang *et al.* [20] showed that for high temperatures, where the dark current substantially exceeds the photocurrent, the internal potentials are in the nanovolt range and therefore cannot be measured anymore. At a sample temperature of 150 K, where the plateaus vanish, the dark current exceeds the maximum photocurrent $I_{\text{ph,max}}$ already

by a factor of 2. This is shown in Fig. 3(b). The maximum photocurrent barely changes with temperature, while the dark current increases exponentially with temperature. I_{dark} was measured at the same voltage as the maximum photocurrent at each temperature. The slight increase in $I_{\text{ph,max}}$ can be explained by changes in the absorption coefficient caused by bandgap narrowing [24]. Taking the derivative of the total photocurrent with respect to the applied bias allows one to determine $\eta_i V_i$ at which the internal fields are compensated, namely, when $\partial I_{\text{ph}}/\partial V$ shows a local maximum that corresponds to the inflection point of the photocurrent. Figures 3(c) and 3(d) show the four $\eta_i V_i$ at different sample temperatures. Towards higher temperatures, the individual values decrease. Above 75 and 100 K no $\eta_3 V_3$ and $\eta_2 V_2$, respectively, can be observed. At temperatures above 150 K, also $\eta_1 V_1$ and $\eta_4 V_4$ vanish because $I_{\text{dark}} > I_{\text{ph}}$. The general trend in Fig. 3(c) closely resembles the results of calculations performed by Huang *et al.* [20] for internal potentials in ICIPs at high operating temperatures.

C. Increased absorber thickness and photocurrent matching

Furthermore, the effect of different absorber lengths on these steps in the photocurrent was studied. For this, three additional four-stage ICIPs were grown by MBE with different individual absorber lengths. The superlattice composition is InAs(2.42 nm)/GaSb(2.14 nm), and the general growth conditions were nominally identical to those for ICIP4-375. ICIP4-500 consists of four identical

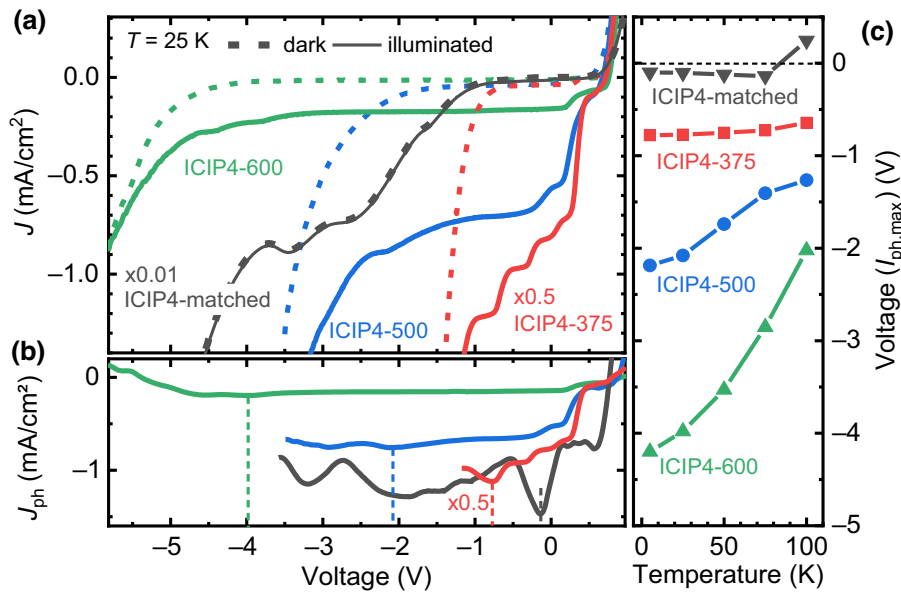


FIG. 4. (a) Current density of the four ICIPs in the dark and under illumination at 25 K. The curves for ICIP4-375 and ICIP4-matched are scaled by factors of 0.5 and 0.01, respectively, for clarity. (b) Photocurrent density of the four ICIPs at 25 K. The external bias necessary to achieve the maximum photocurrent is indicated by the dashed lines. (c) External bias to achieve the maximum photocurrent at different temperatures for the four ICIPs.

stages with individual absorber lengths of 500 nm (109 superlattice periods) and ICIP4-600 consists of four identical 600-nm-thick absorbers (131 superlattice periods). Lastly, a photocurrent-matched ICIP was grown (ICIP4-matched) with individual absorber lengths of 1100, 820, 700, and 600 nm, respectively (240, 180, 153, and 131 superlattice periods, respectively). Photocurrent-matched ICIPs are designed to achieve identical photocurrents in all stages by increasing the absorber thickness towards optically deeper stages to account for light attenuation [20,25–27]. In Fig. 4(a) the current density J of the four ICIPs is shown under dark and illuminated conditions at a sample temperature of 25 K. The curves for ICIP4-375 are offset by a factor 0.5 for clarity, as the photoresponse of ICIP4-375 was larger than that of the other ICIPs. The curves for ICIP4-matched are scaled by a factor of 0.01 as the current density was significantly higher than that of the non-matched ICIPs. This is most probably caused by a larger strain in the superlattice of ICIP4-matched (approximately 550 ppm mismatch to the GaSb substrate) compared with the other ICIPs (0–300 ppm mismatch), resulting in a higher defect density. This is confirmed by the density of surface defects, which is around 2 orders of magnitude larger in ICIP-matched ($6 \times 10^6 \text{ cm}^{-2}$) compared with the other ICIPs (approximately $5 \times 10^4 \text{ cm}^{-2}$). The measurements were performed on ICIP mesas with diameters $d_{\text{ICIP4-500}} = 179 \text{ }\mu\text{m}$, $d_{\text{ICIP4-600}} = 79 \text{ }\mu\text{m}$, and $d_{\text{ICIP4-matched}} = 360 \text{ }\mu\text{m}$.

For all three non-matched ICIPs, plateaus are observed under illumination, while there are none present under dark conditions. Increasing the absorber length results in the Zener-like breakthrough appearing at a larger negative bias. Thicker absorbers require a larger external bias to meet the condition to achieve the Zener-like breakthrough in the ICIP. In addition, the plateaus emerge at

larger negative bias voltages. This is evidenced also in Fig. 4(b), which shows the photocurrent density calculated from Fig. 4(a). Increasing the absorber length results in a larger external bias, i.e., comparable electric fields, required to achieve the maximum photocurrent.

The light attenuation becomes more pronounced when the individual absorber length is increased, as more light is being absorbed in optically first stages. This results in larger internal potentials V_i that require larger external potentials for compensation. In Fig. 4(c) the external bias V_{max} required to achieve the peak photocurrent $I_{\text{ph,max}}$ is shown for different temperatures for all investigated ICIPs. Thicker absorbers require larger external bias to achieve $I_{\text{ph,max}}$. Increasing the temperature results in larger dark currents, which reduce V_i (see also Fig. 3). This also results in smaller V_{max} . Thicker absorbers also result in larger thermal generation and therefore larger dark currents [27]. This is why V_{max} of ICIP4-600 is affected most strongly by temperature, while V_{max} is less sensitive to temperature changes for ICIP4-375.

For ICIP4-matched, plateaulike regions are observed under both dark and illuminated conditions, while no additional plateaus emerge under illumination. This agrees with the proposed model. Instead of variations in the photocurrent generated in individual stages, now the dark current generated in individual stages varies because of the increasing absorber thickness. This also results in internal electric potentials to balance this inequality. The generated photocurrent, however, is equal in each stage as the absorber thickness accounts for light attenuation in preceding stages. Therefore, no additional internal potentials are generated. This results in a peak photocurrent close to zero bias ($V_{\text{max}} \approx 0 \text{ V}$) as can be seen in Figs. 4(b) and 4(c).

In Table I, the figures of merit of the four investigated ICIPs are summarized at room temperature as well

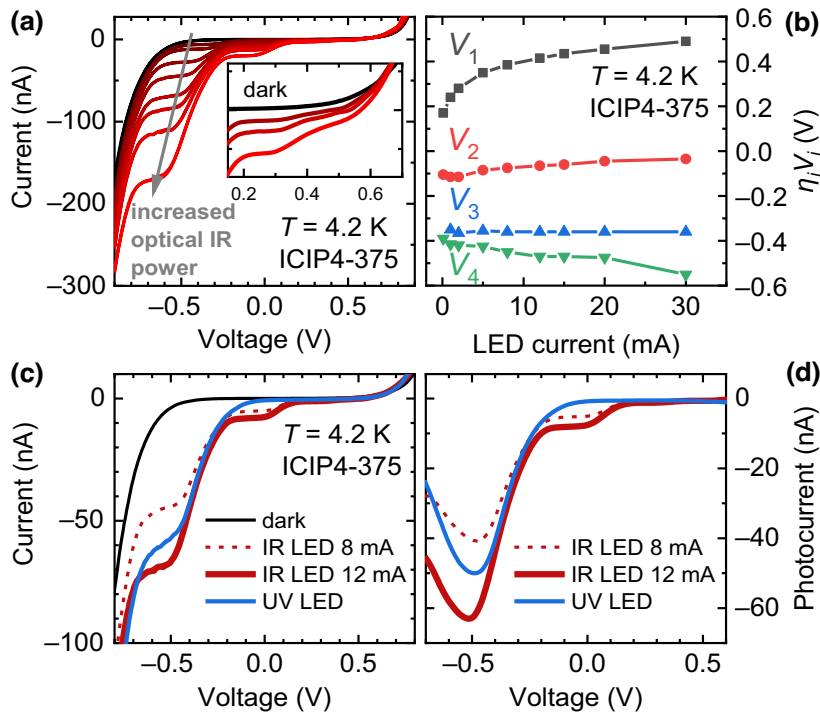


FIG. 5. (a) Dark current and current under different IR illumination powers of ICIP4-375 at $T = 4.2$ K. Four steps in the current emerge that become more prominent when the illumination power is increased. The inset shows an enlargement of the bias range between 0.15 and 0.7 V. (b) Evolution of ηV_i under differing LED current (i.e., illumination power). (c) Comparison between illumination with an IR LED and illumination with a UV LED. Under UV illumination, only one plateau is visible. (d) Photocurrent calculated from (c) for IR and UV illumination.

as at liquid-nitrogen temperature of 77 K. The slight variations of the cutoff wavelength λ_C can be attributed to some growth rate fluctuations in between individual MBE growth runs. The product of differential resistance at zero bias R_0 and mesa area A was calculated from the I - V characteristics. The zero-bias responsivity R_λ at room temperature was measured with a calibrated variable-output-power laser emitting at $5.27 \mu\text{m}$. R_λ at 77 K is provided for a wavelength of $\lambda = 4 \mu\text{m}$ as the cutoff wavelength of some ICIPs dropped below $5.27 \mu\text{m}$ at low temperatures. The specific detectivity at zero bias at $\lambda = 5.27 \mu\text{m}$ (room temperature) and $4.0 \mu\text{m}$ (77 K) was calculated as $D_\lambda^* = R_\lambda \sqrt{R_0 A / 4k_B T}$. For all non-current-matched ICIPs, a specific detectivity of around 2×10^8 Jones was achieved at room temperature. At room temperature, ICIP4-matched outperforms all nonmatched ICIPs by around 50% as it has both the highest $R_0 A$ product and the highest responsivity. At low temperatures, however, the specific detectivity of ICIP4-matched is considerably lower than that of the non-matched ICIPs because of the low $R_0 A$ product related to a higher defect density in the structure.

D. Wavelength dependence and dual-band prospects

As the steps in the photocurrent are related to imbalanced absorption, the wavelength dependence of these steps was studied. For this, ICIP4-375 was mounted in a liquid-helium cryostat, which allows to attach different light-emitting diodes (LEDs) in the vicinity of the ICIP. Varying the LED current changes the optical power incident on the sample. First, at $T = 4.2$ K, the sample

was illuminated with an IR LED emitting light at around 900 nm. The dark current and the current under different illumination levels are shown in Fig. 5(a). Again, four steps in the photocurrent and related plateau regions emerge under illumination, and they become more prominent when the optical power is increased. The inset shows an enlargement of the bias range between 0.15 and 0.7 V to show more clearly the third and fourth steps in the current.

Figure 5(b) shows the evolution of the individual $\eta_i V_i$ as the LED current or optical power is increased. Similar to what was observed in Fig. 3(d), $\eta_1 V_1$ and $\eta_4 V_4$ are affected the most by increases of the optical power, while $\eta_2 V_2$ and $\eta_3 V_3$ remain relatively unchanged. Because of light attenuation, $I_{\text{ph},i}$ is largest in the first stage, resulting in the largest V_i . However, the large V_1 results in a large V_4 supplementing the low photocurrent $I_{\text{ph},4}$ (as indicated in Fig. 2). Therefore, an increasing V_1 also results in an increasing V_4 . From Fig. 5(a) it can be seen that the step height of individual plateaus varies from the ones observed in Fig. 3(a). While all steps in the photocurrent have comparable heights in Fig. 3(a), $I_{\text{ph},i}$ varies considerably in Fig. 5(a). This indicates a wavelength dependence. In Fig. 3, the ICIP was illuminated with an MIR Global light source with peak emission at around $2.5 \mu\text{m}$, while in Fig. 5(a), the sample was illuminated with an LED with an emission wavelength of around 900 nm. As the absorption coefficient increases towards lower wavelengths, the effect of light attenuation becomes more pronounced at $\lambda = 900$ nm. The imbalance between the photocurrent in optically first and last stages increases, as more of the incident light is being absorbed in the first stages. Because

TABLE I. Figures of merit of the four investigated ICIPs, including cutoff wavelength (λ_C), product of differential resistance at zero bias R_0 and area A , and responsivity R_λ and detectivity D_λ^* at $\lambda = 5.27 \mu\text{m}$ at room temperature and 77 K ($\lambda = 4.0 \mu\text{m}$).

Sample	Absorber thickness (nm)	λ_C (μm)		$R_0 A$ ($\Omega \text{ cm}^2$)		R_λ (A/W)		D_λ^* (Jones units)	
		Room temperature	77 K	Room temperature	77 K	Room temperature, 5.27 μm	77 K, 4.0 μm	Room temperature, 5.27 μm	77 K, 4.0 μm
		ICIP4-375	4×375	6.9	5.5	5.9×10^{-2}	8.4×10^3	0.11	0.53
ICIP4-500	4×500	7.0	5.0	6.2×10^{-2}	2.1×10^4	0.12	0.37	2.35×10^8	8.22×10^{11}
ICIP4-600	4×600	6.5	5.0	5.4×10^{-2}	4.5×10^4	0.12	0.38	2.19×10^8	1.24×10^{12}
ICIP4-matched	1100, 820, 700, 600	6.5	4.8	9.1×10^{-2}	1.3×10^3	0.14	0.34	3.32×10^8	1.88×10^{11}

of this, the plateau at $\eta_1 V_1 \approx -0.4 \text{ V}$ ($I_{\text{ph},1}$) in Fig. 5(a) is considerably more pronounced than the others, because $I_{\text{ph},1} \gg I_{\text{ph},2}, I_{\text{ph},3}, I_{\text{ph},4}$. To further investigate this, the IR LED was changed for a UV LED emitting light at around 350 nm. Here the light attenuation should affect the I - V characteristic even more because of the higher absorption coefficient for UV light. In Fig. 5(c) the I - V characteristic under UV illumination is shown together with two I - V curves under illumination with the IR LED. The current on the UV LED was chosen to achieve similar V_1 and $I_{\text{ph},1}$ at the ICIP as under illumination with the IR LED. While for both IR illumination levels plateaus for V_1 and V_2 are clearly visible, under UV illumination only one plateau, for V_1 , can be observed. While a similar photocurrent $I_{\text{ph},1}$ is achieved, because of higher absorption and light attenuation under UV illumination $I_{\text{ph},2}$ is considerably smaller than with IR illumination. Because of this, a second step in the photocurrent corresponding to $I_{\text{ph},2}$ can not be observed under UV illumination. In Fig. 5(d), the photocurrent is shown for the different illumination configurations shown in Fig. 5(c). The photocurrent shows a global maximum at a similar bias of $V = -\eta_1 V_1 \approx -0.5 \text{ V}$ for all illumination levels. This confirms that the observed plateaus at this bias voltage correspond to the photocurrent generated in the first stage. In addition, this feature could also be applied to use the ICIP as a two-color detector. With biasing of the ICIP at $V = -0.5 \text{ V}$, the device is sensitive to both IR radiation and UV radiation, while at $V = 0 \text{ V}$, it is sensitive only to IR radiation. This would allow rapid switching between detecting the IR and UV spectral bands or the IR spectral band by just operating the device in biased mode or unbiased mode. The quantitative limits of this approach require further investigation.

IV. SUMMARY

While ICIPs are commonly designed and optimized for high-operation-temperature applications, low-temperature operation can also be desirable to achieve peak performance by reducing dark currents and noise. This can be especially relevant for applications working with small optical signals requiring low detector noise. At

cryogenic temperatures, steps in the current-voltage characteristic emerge under illumination. These are caused by internal electric potentials building up because of light attenuation and the related variations of generated photocurrent in individual stages of the ICIP. The steps are found to vary with temperature, vanishing once the dark current exceeds the maximum photocurrent. The effect of absorber thickness on these steps was studied. Increasing the individual absorber length increases the disparity of photocurrent generated in individual stages. This leads to the generation of larger internal fields, resulting in a larger external bias required to achieve the maximum photocurrent. Adjustment of the individual absorber lengths in a photocurrent-matched ICIP design results in equal absorption and equal photocurrent in all stages and therefore no internal potentials develop under illumination. Here, however, plateau-like regions are observed that are caused by internal electric potentials that balance inequalities in the generated dark currents in absorbers with differing thickness. Because no additional internal potentials need to be compensated by external bias, no additional steps emerge under illumination and the peak photocurrent is extracted close to zero bias. In addition, the gradual change in photocurrent in individual stages strongly depends on the absorption coefficient. This results in different plateau heights showing different photocurrents $I_{\text{ph},i}$ in the individual stages depending on the incident wavelength and the applied bias. This could potentially be implemented in a two-color-detector approach separating different spectral bands by applying different biases to the ICIP. These results show the importance of taking absorber thickness and absorption coefficient into account when one is designing ICIP structures for different temperature ranges.

ACKNOWLEDGMENTS

This work was funded by the German Ministry of Education and Research (funding program Photonics Research Germany) within the joint research project HISSENS (project funding no. 13N15211) and by the State of Bavaria.

- [1] J. V. Li, R. Q. Yang, C. J. Hill, and S. L. Chuang, Interband cascade detectors with room temperature photovoltaic operation, *Appl. Phys. Lett.* **86**, 101102 (2005).
- [2] A. Bader, F. Hartmann, A. Pfenning, F. Rothmayr, N. Khan, J. Köth, and S. Höfling, in *Infrared Remote Sensing and Instrumentation XXX* Vol. 12233, (SPIE, 2022), p. 122330F.
- [3] E. A. Plis, InAs/GaSb type-II superlattice detectors, *Adv. Electron.* **2014**, 1 (2014).
- [4] A. Rogalski, InAs/GaSb type-II superlattices versus HgCdTe ternary alloys: Future prospect, *Electro-Opt. Infrared Syst. Technol. Appl.* **XIV**, 11 (2017).
- [5] A. Bader, F. Rothmayr, N. Khan, J. Koeth, S. Höfling, and F. Hartmann, Interband cascade infrared photodetectors based on Ga-Free InAs/InAsSb superlattice absorbers, *Appl. Phys. Lett.* **121**, 041104 (2022).
- [6] W. Gawron, L. Kubiszyn, K. Michalczewski, J. Piotrowski, and P. Martyniuk, Demonstration of the longwave type-II superlattice InAs/InAsSb cascade photodetector for high operating temperature, *IEEE Electron Device Lett.* **43**, 1487 (2022).
- [7] C. H. Grein, H. Cruz, M. E. Flatté, and H. Ehrenreich, Theoretical performance of very long wavelength InAs/In_xGa_{1-x}Sb superlattice based infrared detectors, *Appl. Phys. Lett.* **65**, 2530 (1994).
- [8] E. H. Aifer, J. G. Tischler, J. H. Warner, I. Vurgaftman, W. W. Bewley, J. R. Meyer, J. C. Kim, L. J. Whitman, C. L. Canedy, and E. M. Jackson, W-structured type-II superlattice long-wave infrared photodiodes with high quantum efficiency, *Appl. Phys. Lett.* **89**, 1 (2006).
- [9] H. Lotfi, L. Li, L. Lei, Y. Jiang, R. Q. Yang, J. F. Klem, and M. B. Johnson, Short-wavelength interband cascade infrared photodetectors operating above room temperature, *J. Appl. Phys.* **119**, 023105 (2016).
- [10] A. Bader, L. Steinbrecher, F. Rothmayr, Y. Rawal, F. Hartmann, A. Pfenning, and S. Höfling, III–V semiconductor mid-infrared interband cascade light emitters and detectors, *Proc. SPIE* **11830**, 118300E (2021).
- [11] L. Lei, L. Li, H. Lotfi, R. Q. Yang, M. B. Johnson, J. A. Massengale, T. D. Mishima, and M. B. Santos, Long wavelength interband cascade infrared photodetectors operating at high temperatures, *J. Appl. Phys.* **120**, 193102 (2016).
- [12] R. Q. Yang, Z. Tian, Z. Cai, J. F. Klem, M. B. Johnson, and H. C. Liu, Interband-cascade infrared photodetectors with superlattice absorbers, *J. Appl. Phys.* **107**, 054514 (2010).
- [13] H. Lotfi, L. Li, H. Ye, R. T. Hinkey, L. Lei, R. Q. Yang, J. C. Keay, T. D. Mishima, M. B. Santos, and M. B. Johnson, Interband cascade infrared photodetectors with long and very-long cutoff wavelengths, *Infrared Phys. Technol.* **70**, 162 (2015).
- [14] F. Rothmayr, A. Pfenning, C. Kistner, J. Koeth, G. Knebl, A. Schade, S. Krueger, L. Worschech, F. Hartmann, and S. Höfling, Mid-infrared GaSb-based resonant tunneling diode photodetectors for gas sensing applications, *Appl. Phys. Lett.* **112**, 161107 (2018).
- [15] S. Höfling, A. Pfenning, R. Weih, A. Ratajczak, F. Hartmann, G. Knebl, M. Kamp, and L. Worschech, in *Infrared Remote Sensing and Instrumentation XXIV, Proc. SPIE*, Vol. 9973 (2016), p. 997306.
- [16] M. von Edlinger, J. Scheuermann, L. Nähle, L. Hildebrandt, M. Fischer, J. Koeth, R. Weih, S. Höfling, and M. Kamp, in *Imaging and Applied Optics* (Optical Society of America, 2014), pp. paper LTu3D.4.
- [17] R. Rehm, M. Walther, J. Schmitz, J. Fleißner, F. Fuchs, J. Ziegler, and W. Cabanski, InAs/GaSb superlattice focal plane arrays for high-resolution thermal imaging, *Opto-Electron. Rev.* **14**, 19 (2006).
- [18] Hossein Lotfi, Lu Li, Lin Lei, Hao Ye, SM Shazzad Rassel, Yuchao Jiang, and Rui Q. Yang, in *Infrared Technol. Appl. XLII, Proc SPIE* Vol. 9819 (2016), p. 98190Q.
- [19] R. T. Hinkey and R. Q. Yang, Theory of multiple-stage interband photovoltaic devices and ultimate performance limit comparison of multiple-stage and single-stage interband infrared detectors, *J. Appl. Phys.* **114**, 104506 (2013).
- [20] W. Huang, L. Li, L. Lei, J. A. Massengale, R. Q. Yang, T. D. Mishima, and M. B. Santos, Electrical gain in interband cascade infrared photodetectors, *J. Appl. Phys.* **123**, 113104 (2018).
- [21] Z. B. Tian, S. E. Godoy, H. S. Kim, T. Schuler-Sandy, J. A. Montoya, and S. Krishna, High operating temperature interband cascade focal plane arrays, *Appl. Phys. Lett.* **105**, 051109 (2014).
- [22] W. Pusz, A. Kowalewski, P. Martyniuk, W. Gawron, E. Plis, S. Krishna, and A. Rogalski, Mid-wavelength infrared type-II InAs/GaSb superlattice interband cascade photodetectors, *Opt. Eng.* **53**, 043107 (2014).
- [23] W. Huang, L. Li, L. Lei, J. A. Massengale, T. D. Mishima, M. B. Santos, and R. Q. Yang, Gain and resonant tunneling in interband cascade IR photodetectors, *Quantum Sens. Nano Electron. Photonics XV* **10540**, 105400E (2018).
- [24] H. Lotfi, L. Li, S. M. Shazzad Rassel, R. Q. Yang, C. J. Corrège, M. B. Johnson, P. R. Larson, and J. A. Gupta, Monolithically integrated mid-IR interband cascade laser and photodetector operating at room temperature, *Appl. Phys. Lett.* **109**, 151111 (2016).
- [25] K. Hackiewicz, J. Rutkowski, and P. Martyniuk, Long-wavelength interband cascade detector architectures for room temperature operation, *IEEE J. Quantum Electron.* **55**, 4000306 (2019).
- [26] K. Hackiewicz, J. Rutkowski, and P. Martyniuk, Optimal absorber thickness in interband cascade photodetectors, *Infrared Phys. Technol.* **95**, 136 (2018).
- [27] M. B. Santos, L. Li, L. Lei, T. D. Mishima, W. Huang, R. Q. Yang, and J. A. Massengale, Current-matching versus non-current-matching in long wavelength interband cascade infrared photodetectors, *J. Appl. Phys.* **122**, 083102 (2017).